

RUNAWAY M DWARF CANDIDATES FROM THE SLOAN DIGITAL SKY SURVEY

ANDREJ FAVIA¹, ANDREW A. WEST², AND CHRISTOPHER A. THEISSEN²

Draft version November 6, 2018

ABSTRACT

We present a sample of 20 runaway M dwarf candidates (RdMs) within 1 kpc of the Sun whose Galactocentric velocities exceed 400 km s^{-1} . The candidates were selected from the SDSS DR7 M Dwarf Catalog of West et al. (2011). Our RdMs have SDSS+USNO-B proper motions that are consistent with those recorded in the PPMXL, LSPM, and combined *WISE*+SDSS+2MASS catalogs. Sixteen RdMs are classified as dwarfs, while the remaining four RdMs are subdwarfs. We model the Galactic potential using a bulge-disk-halo profile (Kenyon et al. 2008; Brown et al. 2014). Our fastest RdM, with Galactocentric velocity $658.5 \pm 236.9 \text{ km s}^{-1}$, is a possible hypervelocity candidate, as it is unbound in 77% of our simulations. About half of our RdMs have kinematics that are consistent with ejection from the Galactic center. Seven of our RdMs have kinematics consistent with an ejection scenario from M31 or M32 to within 2σ , although our distance-limited survey makes such a realization unlikely. No more than four of our RdMs may have originated from the Leo stream. We propose that to within measurement errors, most of our bound RdMs are likely disk runaways or halo objects, and may have been accelerated through a series of multi-body interactions within the Galactic disk or possibly supernovae explosions.

Keywords: brown dwarfs – proper motions – stars: kinematics and dynamics – stars: late-type – stars: low-mass

1. INTRODUCTION

Recent studies have shown that not all stars within the Milky Way are bound to the Galaxy (Brown et al. 2005; Edelmann et al. 2005; Brown et al. 2006a,b, 2007a,b, 2010, 2012, 2014; Palladino et al. 2014a; Zheng et al. 2014). Tauris (2015) defines genuine hypervelocity stars as those that “will escape the gravitational potential of our Galaxy.” Stellar escape velocity is a function of Galactic position. The escape velocity threshold is $\sim 400 \text{ km s}^{-1}$ in the halo (Kenyon et al. 2008), whereas the current measured escape velocity threshold near the Sun is about $550 \pm 50 \text{ km s}^{-1}$ (Smith et al. 2007; Piffi et al. 2014). Hypervelocity stars are important, because they, unlike the vast majority of stars in the Galaxy, are not bound. One or more mechanisms are thus required to explain their hypervelocity origins. Stars may reach hypervelocity speeds, as predicted by Hills (1988), through a gravitational interaction between a binary system and the central massive black hole (CMBH), in which one of the stars is ejected from the Galaxy while the other is captured into orbit around the CMBH. The hypervelocity stars studied by Brown et al. (2014) and Zheng et al. (2014) have kinematics that are consistent with ejection radially outward from the Galactic center.

Alternative mechanisms may be responsible for observed high Galactocentric (GC) stellar velocities. Edelmann et al. (2005) studied the main-sequence B-type star HE 0437–5439, whose velocity is at least 563 km s^{-1} . Edelmann et al. (2005) showed that if HE 0437–5439 has a GC origin, then its flight time from the center to its current location would be $\sim 100 \text{ Myr}$, about four times longer than its age on the main sequence. Edelmann

et al. (2005) thus proposed a solution that this star is a blue straggler, a blue main-sequence star (such as B type) that persists in clusters beyond the turn-off point of the cluster. Edelmann et al. (2005) suggested that such stars may come into existence through the merger of two lower-mass stars. A related merger-type event between two helium white dwarfs has been proposed to explain the presence of the hypervelocity, subluminescent O-type star US 708 (Hirsch et al. 2005), in the Galactic halo, with a reported GC velocity of $708 \pm 15 \text{ km s}^{-1}$. A more-recent study proposed that the energy of a supernova propelled US 708 outward (Geier et al. 2015) and reported an updated GC velocity of $1157 \pm 53 \text{ km s}^{-1}$. Palladino et al. (2014a) presented a sample of 20 G and K hypervelocity candidates whose kinematics were inconsistent with a CMBH ejection scenario. With the aid of improved proper motion measurements, Ziegerer et al. (2015) dismissed a CMBH ejection scenario for 14 of these stars and concluded that they are likely disk runaways.

While O and B stars may remain on the main sequence for $\sim 10^6 \text{ yr}$, the lowest-mass M dwarfs may remain on the main sequence for $\sim 10^{13} \text{ yr}$ (Laughlin et al. 1997). As M dwarfs (dMs) comprise $\sim 70\%$ of the stars in the Milky Way, they are the dominant stellar constituent (Bochanski et al. 2010). Thus, depending on the mechanism that accelerates these stars to hypervelocities, one might expect to find more hypervelocity M dwarfs than hypervelocity O or B stars. In the last few years, several new studies of hypervelocity candidates later than B-type stars have been published. Li et al. (2012), Palladino et al. (2014a) and Zhong et al. (2014) present hypervelocity candidates of stars as late as K type. However, very few M type hypervelocity stars have been observed to date. Vickers et al. (2015) present 18 hypervelocity candidates ranging in types from F to M. In addition, Savcheva et al.

¹ Department of Physics and Astronomy, University of Maine, Orono, ME 04469

² Department of Astronomy, Boston University, Boston, MA 02215

(2014) includes 14 new hypervelocity M subdwarf candidates with GC velocities exceeding 525 km s^{-1} . Theissen & West (2014) also present a sample of hypervelocity M dwarf candidates.

The primary challenge when observing M dwarfs is their intrinsic faintness, which presents a major limitation for detecting and studying hypervelocity stars. Along the main sequence, B-type stars are $\sim 10^3 - 10^4$ times more luminous than M dwarfs (Habets & Heintze 1981). The low luminosity of M dwarfs also makes spectral and proper motion analysis of M dwarfs particularly challenging. The discovery of runaway M dwarfs would thus provide a significant contribution to the population of identified runaway stars and opens up the possibility of finding hypervelocity M dwarfs. A larger sample of M dwarfs is needed to identify more potential hypervelocity candidates. The spectroscopic catalog of West et al. (2011; hereafter W11) consists of 70,841 visually inspected M dwarfs from the Sloan Digital Sky Survey (SDSS, York et al. 2000) Data Release 7 (DR7, Abazajian et al. 2009). The kinematic data from the W11 catalog thus present an ideal starting point for identifying new hypervelocity candidates.

In this Paper, we present a sample of runaway M dwarf candidates (RdMs) from the W11 catalog. We discuss the process by which we create a high-quality sample of RdM candidates in Section 2. We present the stellar properties of our RdMs and determine the probabilities for each of our RdMs to be bound or unbound in Section 3. We discuss selection effects and possible acceleration mechanisms for our RdMs in Section 4. We summarize our Paper in Section 5.

2. DATA

2.1. Background

The stars in W11 were inspected using the Hammer spectral typing facility (Covey et al. 2007) to determine spectral types and ensure that extragalactic interlopers were excluded. Stars were included only if they had $S/N \geq 3$ at $\sim 8300 \text{ \AA}$. Proper motions of the stars in W11 were extracted from the SDSS+USNO-B proper motion catalog (Munn et al. 2004, 2008). Distances were calculated using the photometric parallax relation between M_r and the extinction-corrected $r - z$ color of the star (Bochanski et al. 2010). Heliocentric radial velocities (RVs) were determined by cross-correlating each spectrum with a template for that subtype, yielding typical precisions of $7-10 \text{ km s}^{-1}$ (Bochanski et al. 2007, hereafter B07b). The M dwarfs in the W11 catalog were categorized based on whether they passed a set of processing flags, described below.

Proper motions are essential in measuring the tangential velocities (TVs) of M dwarfs. The hypervelocity O and B-type stars previously studied are mostly RV validated, whereas nearby RdMs can have high RVs, high proper motions, or both. Proper motions for stars in the W11 catalog were pulled from the proper motion catalog of Munn et al. (2004, 2008). We adopted a set of clean proper motion flags established by Kilic et al. (2006), which enabled large, statistically complete samples of white dwarfs from SDSS. Several of their processing flags include: `match`, the number of objects in USNO-B which match an SDSS object in a $1''$ radius; `sigRA` & `sigDec`,

the residuals in the linear fit (based on all epochs at which the object was observed) of right ascension and declination proper motions; `nFit`, the number of detections between SDSS and USNO-B used in the fit, with a maximum of 6; and `dist22`, the angle (in arcsec) to the nearest neighbor in SDSS with $g < 22$.

The distribution of proper motion errors in Munn et al. (2004), who required `match = 1`, `sigRA` & `sigDec` < 350 , and `nFit` ≥ 4 , can be assessed by examining the proper motions of quasars. Munn et al. (2004) state that “objects detected on fewer than four plates in USNO-B suffer from a large contamination by false matches.” According to Dong et al. (2011), contamination in the sample can be reduced by requiring `match = 1`, `sigRA` & `sigDec` < 525 (the condition for the residuals is relaxed), `nFit` = 6, and `dist22` > 7 . The condition `nFit` = 6, according to Dong et al. (2011), “makes the cleanness of our samples much better than that of samples defined using the standard criteria defined by Munn et al. (2004), even when we loosen the requirement on rms fitting residuals a little bit.” For comparison, the processing flags adopted by W11 include: `GOODPHOT`, which equals 1 if the distances are defined by the photometry and have measured magnitudes, 0 otherwise; `GOODPM`, which equals 1 if the proper motions satisfy the conditions `match = 1`, `dist22` > 7 , `sigRA` & `sigDec` < 1000 , and (`nFit` = 6 or (`nFit` = 5 and (`O` < 2 or `J` < 2))) Munn et al. (2004), 0 otherwise (see footnote 13 in West et al. 2011); and `WDM`, which equals 1 for a possible white dwarf-M dwarf pair, 0 otherwise.

Proper motions in the SDSS+USNO-B catalog combine relative proper motions from observations taken on USNO-B plates with SDSS CCD photometry. Stellar proper motions are also recorded in other catalogs, such as the Positions and Proper Motions catalog (PPMXL Roeser et al. 2010), the Lépine Shara Proper Motion catalog (LSPM, Lépine & Shara 2005), which was inspected by eye, and the *Wide-field Infrared Survey Explorer* (*WISE*, Wright et al. 2010), which is tied to the International Coordinate Reference System (ICRS) through the Two-Micron All-Sky Survey (2MASS, Skrutskie et al. 2006). Dong et al. (2011) investigated the proper motion error distribution of the SDSS+USNO-B catalog using quasars, as they have extragalactic distances and so are expected to exhibit no observable proper motion. Using the 10th release of the SDSS quasar catalog (Pâris et al. 2014), Dong et al. (2011) found that the proper motion errors of quasars are well represented by a distribution consisting of a Gaussian core with extended wings.

The catalog by Theissen et al. (submitted) established updated proper motions for $\gtrsim 10^6$ KML stars from a combination of SDSS, *WISE*, and 2MASS baselines. The choice to adopt a baseline depended on whether or not each source passed a set of processing flags. Within their catalog, processing flags from among the SDSS, *WISE*, and 2MASS catalogs were applied to the SDSS quasar catalog to define a set of QSOs. These were used to compute angular distances between catalog baselines and provide updated proper motion errors for KML stars, depending on the number of observation epochs for that star.

2.2. Initial Sample

Data are taken from the W11 spectroscopic catalog, which consists of 70,841 visually inspected M dwarfs from the SDSS (York et al. 2000) DR7 (Abazajian et al. 2009). The proper motions in the W11 catalog are based on Munn et al. (2004), which omits proper motions $\gtrsim 300$ mas yr⁻¹. We thus retrieved proper motions for 47 high proper motion stars using the Theissen et al. 2015 (submitted) catalog, in which combinations of SDSS, *WISE*, and 2MASS baselines determined updated proper motions for these RdM candidates.

Magnitudes in W11 are extinction-corrected using the method of Schlegel et al. (1998). These corrections rely on column densities calculated from 100 and 240 μ m Galactic emission along the line-of-sight out to infinity, and therefore may overestimate the true extinction to nearby stars. Jones et al. (2011) provides a more robust Galactic extinction map by fitting extinction curves to the fluxes of $\sim 56,000$ M dwarfs in the spectral range 5700–9200 Å from the W11 catalog. We correct for extinction using the method of Jones et al. (2011), except for M dwarfs not present in the Jones et al. (2011) catalog, where we apply the extinction corrections of Schlegel et al. (1998). Extinction corrections from the Jones et al. (2011) catalog were available for 57,067 stars. The mean extinction correction for our final sample is 0.18 magnitudes. Given that the mean apparent magnitude of our sample is $\langle r \rangle = 17.1$, and the mean distance from the Sun is 686 pc, our stellar distances would have been offset by $\sim 8.6\%$ if extinction corrections using either catalog are neglected. Most of our other uncertainties (e.g., metallicity, spread in the photometric parallax relationship), are typically larger than this, so the effect of extinction on distance is minimal in comparison.

2.3. Distances and Kinematics

Because trigonometric parallaxes are not available for many faint stars, such as M dwarfs, alternate relations must be employed. (Bochanski et al. 2010) derived a photometric parallax relation between M_r and the extinction-corrected $r-z$ color of the star. Given two different filters, the color of a star determines its distance in a particular band λ using the distance modulus relation

$$m_{\lambda_1} - M_{\lambda_1}(m_{\lambda_1} - m_{\lambda_2}) = 5 \log d - 5, \quad (1)$$

where d is the distance, m_{λ_1} is the apparent magnitude in one filter, $m_{\lambda_1} - m_{\lambda_2}$ is the color from two filters, and M_{λ_1} is the absolute magnitude, which is a function of the color. Using a sample of nearby stars with known absolute magnitudes derived from trigonometric parallax relations, Bochanski et al. (2010) derived the photometric parallax relation

$$M_r = 5.190 + 2.474(r-z) + 0.4340(r-z)^2 - 0.08635(r-z)^3, \quad (2)$$

and the residual rms scatter in the relation is 0.394. Distances in the W11 catalog were calculated using this photometric parallax relation.

As first described by Sandage & Eggen (1959), lower-metallicity stars will have higher surface temperatures and thus higher luminosities than higher-metallicity stars of the same mass. Corrections to the absolute magnitude may be derived using iron abundance (e.g., Ivezić et al. 2008). As Bochanski et al. (2013) demonstrate, the photometric parallax relation must be modified for the lower

Table 1
M Subdwarf Model Parameters^a

Class	$r-z$	M_r	σ_M
sdM	1.05	10.0996	0.422153
	1.35	10.5971	0.422138
	1.65	11.5888	0.422124
	1.95	12.9130	0.422156
	2.25	13.3980	0.422160
esdM	1.05	9.98573	0.421217
	1.35	11.4767	0.420383
	1.65	12.5346	0.421741
usdM	1.05	11.1409	0.415195
	1.35	12.1264	0.413827

^a Figure 4a of Bochanski et al. (2013)

metallicity classes (subdwarfs, extreme subdwarfs, and ultra subdwarfs). By taking metallicity into account, which we do in this study, the distance uncertainties are actually reduced. However, precise metallicities for many M subdwarfs have not been measured, and instead proxies for metallicities have been developed to establish metallicity classes. These classes are parameterized by the metallicity-dependent quantity ζ , which is a relation between the CaH and TiO molecular indices (Dhital et al. 2012). The indices upon which ζ are based have been employed as temperature and metallicity indicators for low-mass stars (Bochanski et al. 2007, and references therein). The parameter ζ is calibrated over spectral types M0–M3, but suffers from large spreads near solar metallicity (Woolf et al. 2009). Lépine et al. (2007) classified stars as subdwarfs, extreme subdwarfs, and ultra subdwarfs, for ζ in the ranges 0.5 – 0.825, 0.2 – 0.5, and less than 0.2, respectively.

For stars with $\zeta > 0.825$ (dwarfs), we use the photometric parallax relation of Bochanski et al. (2010), which provides distance uncertainties of $\sim 20\%$ due to scatter along the main sequence. This is a conservative estimate, since no metallicity information was used to derive the photometric parallax relation. For stars of lower metallicity classes, we adopt empirical models of M_r vs. $r-z$ using the results of Bochanski et al. (2013). Specifically, we adopt the models in Figure 4a of Bochanski et al. (2013), which presents separate empirical fits for subdwarfs, extreme subdwarfs, and ultra subdwarfs. Table 1 presents the parameters that Bochanski et al. (2013) derived for their M subdwarf models (J. J. Bochanski, private communication).

The discrepancy in M_r between metallicity subclasses is ~ 1 magnitudes, which for a subdwarf with apparent magnitude $r = 20$, translates to a distance discrepancy of ~ 0.2 kpc. Bochanski et al. (2010, 2013) find that the scatter in their parallax relations is $\sigma_M \sim 0.4$. To simulate the distance errors due that would result from variation in ζ , we perform Monte Carlo simulations with 1000 realizations on r , $r-z$, ζ , and the extinction values, assuming normally-distributed errors. Our final sample has a mean distance uncertainty of $\sim 26\%$, primarily due to variation in ζ .

The RVs, distances, and proper motions from Munn et al. (2004, or if missing, Theissen et al., submitted) were used to calculate the U, V, W velocities of each star, where U points from the Sun toward the Galactic center parallel to the midplane, V points in the direction projected from the Sun’s velocity onto the mid-

plane, and W points directly north of the midplane. Following the convention of Zheng et al. (2014), we adopt 250 km s^{-1} for the velocity of the Local Standard of Rest (LSR; Reid et al. 2009; McMillan & Binney 2010) and $(U_0, V_0, W_0) = (11.1, 12.24, 7.25) \text{ km s}^{-1}$ for the peculiar motion of the Sun with respect to the LSR (Schönrich et al. 2010). Throughout this Paper, we include dwarfs, subdwarfs, extreme subdwarfs, and ultra subdwarfs in our definition of runaway M dwarf candidates (RdMs).

For the purpose of constructing a high quality sample of RdMs from W11, we kept stars that had flags set to $\text{GOODPHOT} = 1$, $\text{GOODPM} = 1$, and $\text{WDM} = 0$. We also relaxed the criterion on nFit and include stars down to $\text{nFit} = 4$. We excluded stars whose S/N of the spectrum near $H\alpha$ was less than 3. To ensure that our sample contains stars with low proper motion uncertainties, we also culled from our sample all stars farther than 1 kpc from the Sun. Based on the provided distances, proper motions, and RVs, we constructed a reduced sample of 196 RdMs whose GC velocities exceed 400 km s^{-1} .

2.4. Spectra

To confirm the RVs for the RdM candidates, we inspected two sets of sodium absorption transitions present in the spectra of the RdMs. Appendix A presents the sodium transitions under consideration, and their rest frame wavelengths in vacuum. We visually examined the Doppler shift of these sodium transitions to validate the RV measurements. Heliocentric RVs and their uncertainties, recorded in W11, were determined using the method of B07b. Some of our RdMs had RV uncertainties in the W11 catalog exceeding 100 km s^{-1} . We thus applied an alternative cross-correlation function (CCF) routine to estimate an additional RV uncertainty. We first determined the spectral type (e.g., M0) of each RdM and splined its corresponding template to the SDSS resolution. We cross-correlated the SDSS spectrum with the template in five wavelength windows and splined the cross-correlation function (CCF) to determine the lag at which the CCF is a maximum. The windows range from 6531 to 7760 Å in step sizes of $0.0150 \log(\text{Å})$, or $\sim 250 \text{ Å}$. Our justification for these windows is that M dwarf SDSS optical spectra tend to have higher S/N ratios toward the red end (Jones et al. 2011), which produces smaller variations in the lag. We calculate the standard error of the lags about their mean to determine the RV uncertainty.

We retained stars with clearly discernible sodium transitions in their spectra and RV discrepancies within a 2σ RV uncertainty window. As a result of our visual inspection, we arrived at a refined sample of 33 RdMs. Figure 1 shows an example of the SDSS optical spectrum of J184314.08+412258.9, an M0, whose GC velocity is $427.2 \pm 107.8 \text{ km s}^{-1}$ and whose RV is $-317.1 \pm 6.6 \text{ km s}^{-1}$. Figure 1 also presents a close-up of the spectrum in the vicinity of the 3p→3d Na triplet (8185.51, 8197.05, and 8197.08 Å).

2.5. Proper Motions

To investigate the robustness of our proper motions, we compared the proper motions for our RdMs from SDSS+USNO-B (used in W11), PPMXL (Roeser et al. 2010), LSPM (Lépine & Shara 2005), and a master catalog (hereafter *WISE*+SDSS+2MASS; Theissen et al.,

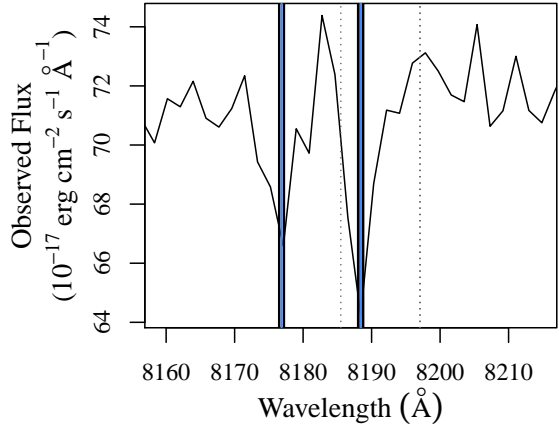


Figure 1. Close-up of the SDSS optical spectrum of J184314.08+412258.9, an M0, with Galactocentric velocity $427.2 \pm 107.8 \text{ km s}^{-1}$ and radial velocity $-317.1 \pm 6.6 \text{ km s}^{-1}$, in the vicinity of the 3p→3d Na triplet. The dotted gray lines located at 8185.51, 8197.05, and 8197.08 Å indicate the rest frame transitions in vacuum. The solid blue lines and the neighboring solid black lines indicate the expected Doppler-shifted wavelengths of the transitions and 2σ uncertainties in the RV, respectively.

submitted), which combines data from *WISE* (Wright et al. 2010), SDSS, and 2MASS (Skrutskie et al. 2006). For LSPM proper motion errors, we adopt the quoted velocity dispersion based on SUPERBLINK astrometry (see Section 5.2 of Lépine & Shara (2005)) to give 2σ errors of $(\mu_\alpha = 14.6, \mu_\delta = 12.6) \text{ mas yr}^{-1}$. In making our comparisons, we considered whether the SDSS+USNO-B proper motions shared a 2σ overlap with the proper motions of the other catalogs. The *WISE*+SDSS+2MASS baselines are tied to the ICRS, whereas five of the six SDSS+USNO-B epochs use relative positions and proper motions. From our sample, we removed four RdMs whose SDSS+USNO-B proper motions were inconsistent with those of *WISE*+SDSS+2MASS. LSPM proper motions were available for 13 of the remaining 20 RdMs. Table 2 presents the measured proper motions and 2σ errors based on the various catalogs under consideration. Table 2 shows that the proper motions are generally consistent among the catalogs to within the uncertainties.

3. RESULTS

3.1. Properties

Our final sample consists of 20 RdMs with high-quality SDSS spectra. We present the properties of our RdMs in Table 3, where M is the spectral type, ζ is the metallicity-dependent parameter discussed in Section 2.3, r is the r -band PSF magnitude, extinction-corrected using the method of Jones et al. (2011; or Schlegel et al. 1998 if the RdM was not in the Jones et al. (2011) catalog), D is the distance, RV is the heliocentric radial velocity, U, V, W are the velocity components in the Galactic coordinate system, computed using the SDSS+USNO-B proper motions of Munn et al. (2004), TV is the tangential velocity (proper motion scaled to distance), v_{tot} is the velocity of the star with respect to the Galactic center, and μ is the SDSS+USNO-B proper motion in right ascension (α , already corrected for declination in Munn et al. 2004) and declination (δ). Uncertainties in v_{tot} were calculated by adding the uncertainties in U, V, W in quadrature. Reported RV uncertainties are the lesser of those calculated by Bochanski et al. (2010) or our CCF routine, outlined

Table 2
Proper Motions for our Runaway M Dwarf Candidates

RdM	Name	R.A. (deg.)	Dec. (deg.)	SDSS+USNO-B ^a μ_α (mas yr ⁻¹)	μ_δ (mas yr ⁻¹)	PPMXL ^b μ_α (mas yr ⁻¹)	μ_δ (mas yr ⁻¹)	WISE+SDSS+2MASS ^c μ_α (mas yr ⁻¹)	μ_δ (mas yr ⁻¹)	LSPM ^d μ_α (mas yr ⁻¹)	μ_δ (mas yr ⁻¹)
1	J003012.87-184446.9	7.5536	-18.74638	-78.3 ± 5.3	-148.5 ± 5.3	-68.4 ± 7.2	-151.2 ± 7.2	-99.9 ± 17.4	-161.2 ± 18.7
2	J023510.64+004924.9	38.7944	0.82359	17.3 ± 6.2	-183.7 ± 6.2	18.0 ± 7.2	-183.6 ± 7.2	32.7 ± 21.9	-172.9 ± 20.3	25	-188
3	J035310.50-004928.1	58.2938	-0.82447	63.7 ± 6.2	-149.4 ± 6.2	68.4 ± 7.2	-144.0 ± 7.2	55.6 ± 29.6	-155.3 ± 67.4
4	J100557.07+344549.0	151.4878	34.70363	-351.8 ± 5.6	-255.7 ± 5.6	-356.4 ± 7.2	-255.6 ± 7.2	-347.0 ± 22.8	-256.2 ± 24.4	-361	-256
5	J110252.68+274203.7	165.7195	27.70104	27.5 ± 5.6	-146.0 ± 5.6	25.2 ± 7.2	-144.0 ± 7.2	30.4 ± 37.9	-156.8 ± 20.6	30	-158
6	J111825.99+090229.4	169.6083	9.04152	-201.9 ± 5.4	-80.6 ± 5.4	-201.6 ± 7.2	-75.6 ± 7.2	-200.6 ± 23.6	-86.4 ± 23.4	-178	-87
7	J120525.80+403509.8	181.3575	40.58607	-121.3 ± 6.2	-60.2 ± 6.2	-122.4 ± 7.2	-57.6 ± 7.2	-118.3 ± 16.3	-68.3 ± 22.2
8	J121441.21+414924.8	183.6717	41.82356	-516.9 ± 6.4	-447.4 ± 6.4	-518.4 ± 7.2	-446.4 ± 7.2	-524.8 ± 24.9	-442.3 ± 19.0	-525	-430
9	J131702.01+382435.2	199.2584	38.40978	-168.7 ± 6.0	9.6 ± 6.0	-169.2 ± 7.2	7.2 ± 7.2	-172.4 ± 32.9	-7.0 ± 45.4	-163	-9
10	J140921.10+370542.6	212.3379	37.09518	-152.6 ± 5.4	-73.9 ± 5.4	-154.8 ± 7.2	-75.6 ± 7.2	-146.3 ± 47.8	-77.2 ± 24.0	-154	-80
11	J142546.68+082717.2	216.4445	8.45480	-46.9 ± 5.4	-197.7 ± 5.4	-54.0 ± 7.2	-198.0 ± 7.2	-54.3 ± 20.3	-209.3 ± 37.9	-56	-202
12	J153737.72-005608.7	234.4072	-0.93575	-4.5 ± 5.5	55.3 ± 5.5	0.0 ± 7.2	54.0 ± 7.2	-39.2 ± 137.7	-36.9 ± 139.3
13	J182547.07+641355.5	276.4462	64.23209	45.2 ± 5.4	138.9 ± 5.4	39.6 ± 7.2	136.8 ± 7.2	55.2 ± 57.9	158.2 ± 34.3	43	143
14	J184314.08+412258.9	280.8087	41.38304	-52.8 ± 5.4	121.0 ± 5.4	-54.0 ± 7.2	118.8 ± 7.2	-51.5 ± 14.8	120.1 ± 17.2
15	J203803.39+145300.2	309.5142	14.88341	-64.7 ± 5.6	-128.1 ± 5.6	-64.8 ± 7.2	-129.6 ± 7.2	-40.3 ± 28.0	-139.6 ± 21.8	-60	-143
16	J221152.95+002207.7	332.9706	0.36882	-104.9 ± 5.7	-232.5 ± 5.7	-104.4 ± 7.2	-234.0 ± 7.2	-122.6 ± 16.8	-237.2 ± 20.0	-104	-230
17	J224403.71+231532.4	341.0155	23.25902	348.5 ± 5.7	-32.2 ± 5.7	349.2 ± 7.2	-39.6 ± 7.2	352.1 ± 13.2	-20.6 ± 15.1	349	-27
18	J231405.61+230120.2	348.5234	23.02229	119.9 ± 5.7	11.2 ± 5.7	122.4 ± 7.2	10.8 ± 7.2	117.2 ± 46.7	7.0 ± 15.1
19	J232541.30+000419.6	351.4221	0.07211	453.3 ± 5.7	-118.8 ± 5.7	450.0 ± 7.2	-118.8 ± 7.2	457.6 ± 17.8	-111.4 ± 20.6	457	-114
20	J235459.63-004133.2	358.7485	-0.69257	-88.8 ± 5.7	-69.4 ± 5.7	-90.0 ± 7.2	-75.6 ± 7.2	-72.8 ± 15.4	-69.4 ± 15.9

^a Munn et al. (2004)

^b Roeser et al. (2010)

^c Theissen et al., submitted

^d Lépine & Shara (2005); typical 2σ errors are $\sigma_{\mu_\alpha} = 14.6$ mas yr⁻¹ and $\sigma_{\mu_\delta} = 12.6$ mas yr⁻¹.

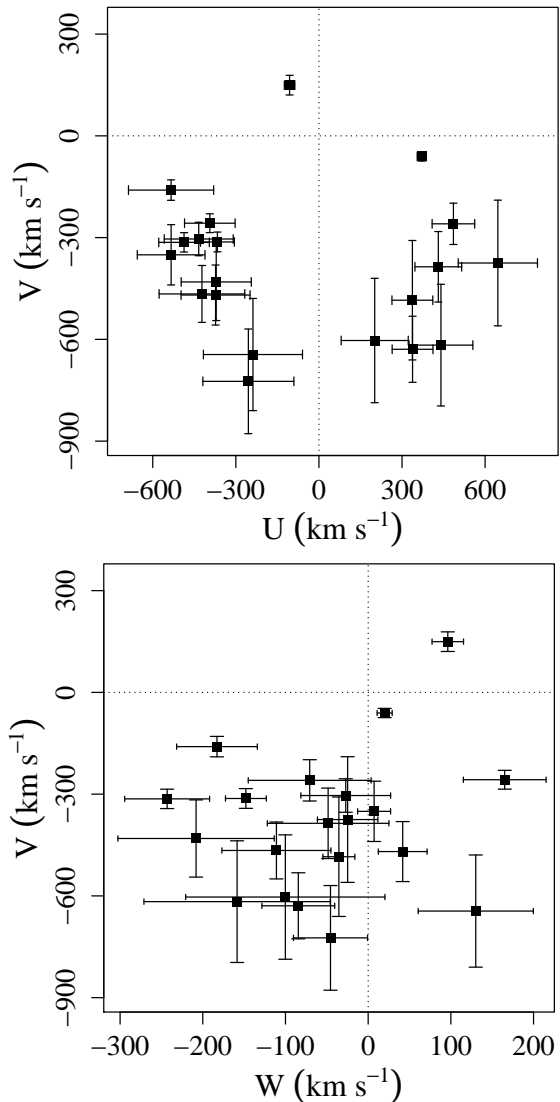


Figure 2. Kinematic distribution of our runaway M dwarf candidates, with 1σ error bars in each velocity component. Our sample generally consists of stars with $|U| > 200 \text{ km s}^{-1}$ and $V < 0 \text{ km s}^{-1}$, but no preferred speed in W .

in Section 2.4. The uncertainty in ζ for RdM 3 is large; generally, the $[\text{Fe}/\text{H}]-\zeta$ relation has considerable scatter at the high-metallicity end of the relation (Woolf et al. 2009). As Figure 3 shows, the RdM 5 spectrum has comparable S/N to the spectra of our other candidates, so we attribute the high ζ uncertainty to scatter at the high metallicity end of the $[\text{Fe}/\text{H}]-\zeta$ relation.

Figure 2 shows the V vs. U and V vs. W kinematics of our sample, with 1σ error bars in each velocity component. The majority of our RdMs have V velocities that are moving in the opposite direction of Galactic rotation. With the exception of RdM 4, our sample consists of RdMs with U speeds exceeding 200 km s^{-1} . Our sample generally consists of stars with $|U| > 200 \text{ km s}^{-1}$ and $V < 0 \text{ km s}^{-1}$, but no preferred speed in W . Our W velocity dispersion is much lower than our U or V velocity dispersion. We discuss the implications on our tangential velocities in Section 4.2.

Figure 3 presents the optical spectra of our RdM sample in the range $5000 - 9000 \text{ \AA}$. All of our spectra show

clear TiO features. The extreme subdwarf RdMs 4, 8, 17, and 19 show a significant reduction in the TiO band, as is expected in the spectrum of extreme subdwarfs (Savcheva et al. 2014). The $3s \rightarrow 3p$ Na doublet is particularly prominent in the spectrum of each RdM, while the $3p \rightarrow 3d$ Na triplet stands out less in the spectrum of most of our RdMs.

3.2. Are the RdMs Bound to the Galaxy?

To test whether each of the 20 RdMs are bound to the Milky Way, we adopt the three-component bulge-disk-halo model of Kenyon et al. (2008), as it is well suited to study the kinematics of hypervelocity candidates. For GC distance r , GC radius R (that is, r projected onto the Galactic plane), and height z above the plane, the Galactic potential is given by

$$\Phi = \Phi_b + \Phi_d + \Phi_h, \quad (3)$$

where the potentials for the bulge, disk, and halo are respectively given by

$$\begin{aligned} \Phi_b(r) &= -GM_b/(r + a_b), \\ \Phi_d(R, z) &= -GM_d/\sqrt{R^2 + [a_d + (z^2 + b_d^2)^{1/2}]^2}, \\ \Phi_h(r) &= -GM_h \ln(1 + r/r_s)/r. \end{aligned} \quad (4)$$

We adopt the parameters used by Kenyon et al. (2008) and update the values of the disk mass M_d and radial scale length r_s to be in closer agreement with the observed mass measurements of the Milky Way (Brown et al. 2014). The parameters of our model are given in Table 4.

For each star, we perform a semi-Euler (symplectic) integration using the 3D positions and velocities of the RdMs as our initial conditions, and time steps of 10^5 yr . Symplectic integration has been used to simulate the interaction between a binary system and the CMBH (Bromley et al. 2006) for the purpose of studying hypervelocity candidates (Kenyon et al. 2008), and to model the orbital dynamics of the giant planets in the early solar system (Morbidelli et al. 2007). We classify each RdM as bound or unbound by integrating until:

1. the star reaches the Galactic virial radius (R_{vir}) of 250 kpc (see Section 4.2 of Brown et al. 2014),
2. the star, once gaining distance from the Galactic center, reaches a turnaround distance within R_{vir} , or
3. a total of 2.5 Gyr (25,000 steps) elapses without either of the previous conditions being met.

All of our RdMs ultimately meet either the first or the second condition. Table 5 presents the results of our integrations. We consider an RdM “unbound” if it reaches R_{vir} within 2.5 Gyr. For each unbound RdM, we report the escape time t_{esc} , which is how long the RdM is expected to take to reach R_{vir} . Alternatively, for each bound RdM, we report the maximum distance R_{max} from the Galactic center. The column “% Unbound” represents the percentage of our simulations, which we describe in Section 3.3, in which the RdM reaches R_{max} .

Table 3
Properties of our Runaway M Dwarf Candidates

RdM	Name	M (SpT)	ζ^a	r	D (pc)	RV (km s ⁻¹)	U (km s ⁻¹)	V (km s ⁻¹)	W (km s ⁻¹)	TV (km s ⁻¹)	v_{tot} (km s ⁻¹)
1	J003012.87-184446.9	0	1.02 ± 0.46	17.22 ± 0.09	934 ± 296	-36.6 ± 17.8	646.0 ± 143.0	-374.9 ± 185.3	-24.8 ± 36.5	743.4 ± 236.2	658.5 ± 236.9
2	J023510.64+004924.9	0	0.83 ± 0.23	17.10 ± 0.04	862 ± 275	-198.5 ± 9.5	440.5 ± 115.2	-616.9 ± 179.3	-158.5 ± 112.7	753.9 ± 240.9	594.9 ± 241.1
3	J035310.50-004928.1	0	4.20 ± 11.20	17.33 ± 0.10	848 ± 325	2.0 ± 1.5	201.4 ± 121.0	-603.4 ± 183.3	-100.2 ± 120.5	653.3 ± 250.5	418.9 ± 250.5
4	J100557.07+344549.0	0	0.24 ± 0.08	16.32 ± 0.09	299 ± 93	93.5 ± 29.1	-370.9 ± 126.5	-430.8 ± 113.8	-208.1 ± 94.5	616.3 ± 192.4	462.1 ± 194.6
5	J110252.68+274203.7	0	0.87 ± 0.59	17.09 ± 0.05	840 ± 271	-72.8 ± 11.0	337.4 ± 73.7	-484.6 ± 176.1	-35.4 ± 19.3	591.5 ± 191.5	412.5 ± 191.9
6	J111825.99+090229.4	0	0.84 ± 0.09	17.03 ± 0.03	611 ± 182	184.7 ± 11.4	-422.4 ± 154.7	-466.0 ± 83.9	-110.9 ± 65.9	629.7 ± 187.6	487.2 ± 187.9
7	J120525.80+403509.8	0	1.01 ± 0.21	17.36 ± 0.04	954 ± 240	74.8 ± 5.1	-373.2 ± 124.6	-469.3 ± 88.5	41.8 ± 29.5	612.6 ± 155.5	434.9 ± 155.6
8	J121441.21+414924.8	1	0.24 ± 0.06	17.44 ± 0.11	240 ± 71	-98.5 ± 5.6	-254.8 ± 164.3	-723.8 ± 154.3	-45.5 ± 44.8	778.2 ± 229.8	539.9 ± 229.8
9	J131702.01+382435.2	1	0.89 ± 0.08	18.07 ± 0.02	814 ± 188	-58.9 ± 13.1	-533.7 ± 122.2	-350.7 ± 88.8	7.2 ± 19.9	652.0 ± 151.8	543.1 ± 152.4
10	J140921.10+370542.6	0	1.31 ± 3.43	17.26 ± 0.04	876 ± 314	-115.2 ± 5.5	-238.2 ± 178.9	-644.7 ± 165.4	130.1 ± 69.6	704.0 ± 253.3	479.0 ± 253.3
11	J142546.68+082717.2	0	1.84 ± 0.79	17.12 ± 0.01	747 ± 134	92.7 ± 10.6	338.0 ± 73.7	-629.2 ± 97.4	-84.5 ± 44.0	719.9 ± 129.4	515.0 ± 129.8
12	J153737.72-005608.7	1	0.97 ± 0.12	17.80 ± 0.02	761 ± 138	-20.6 ± 6.5	-106.0 ± 19.0	149.5 ± 28.9	96.3 ± 19.0	200.2 ± 38.9	424.4 ± 39.5
13	J182547.07+641355.5	0	0.95 ± 0.29	17.31 ± 0.03	818 ± 236	-206.0 ± 4.8	-533.9 ± 153.8	-159.9 ± 30.1	-182.8 ± 48.8	566.0 ± 164.1	571.5 ± 164.1
14	J184314.08+412258.9	0	1.14 ± 0.46	16.64 ± 0.06	642 ± 171	-317.1 ± 6.6	-393.9 ± 91.3	-257.5 ± 27.7	165.1 ± 50.0	401.5 ± 107.6	427.2 ± 107.8
15	J203803.39+145300.2	0	1.16 ± 0.31	17.12 ± 0.01	810 ± 179	30.3 ± 4.4	485.6 ± 76.9	-259.4 ± 60.9	-70.7 ± 74.3	551.4 ± 123.0	490.8 ± 123.0
16	J221152.95+002207.7	0	0.96 ± 0.18	16.25 ± 0.01	477 ± 126	-75.0 ± 7.0	431.0 ± 84.4	-386.0 ± 103.9	-48.4 ± 73.5	576.6 ± 152.5	454.6 ± 152.7
17	J224403.71+231532.4	0	0.46 ± 0.11	16.85 ± 0.04	377 ± 65	-161.9 ± 2.5	-487.0 ± 91.3	-314.0 ± 28.6	-243.1 ± 51.3	625.3 ± 108.5	548.1 ± 108.5
18	J231405.61+230120.2	0	2.03 ± 1.34	17.39 ± 0.08	889 ± 251	-204.6 ± 5.6	-434.1 ± 124.5	-304.1 ± 49.3	-27.1 ± 54.3	507.5 ± 144.4	438.3 ± 144.5
19	J232541.30+000419.6	1	0.42 ± 0.08	16.84 ± 0.06	232 ± 32	-80.8 ± 6.6	-366.6 ± 61.1	-312.8 ± 29.1	-147.9 ± 24.7	515.6 ± 71.8	400.2 ± 72.1
20	J235459.63-004133.2	0	1.36 ± 0.22	17.09 ± 0.02	680 ± 35	-57.9 ± 5.9	371.4 ± 16.6	-60.8 ± 13.6	20.0 ± 9.1	363.3 ± 22.6	417.3 ± 23.3

^a ζ is defined as in Lépine et al. (2007), where subdwarfs, extreme subdwarfs, and ultra subdwarfs, for ζ in the ranges 0.5 – 0.825, 0.2 – 0.5, and less than 0.2, respectively.

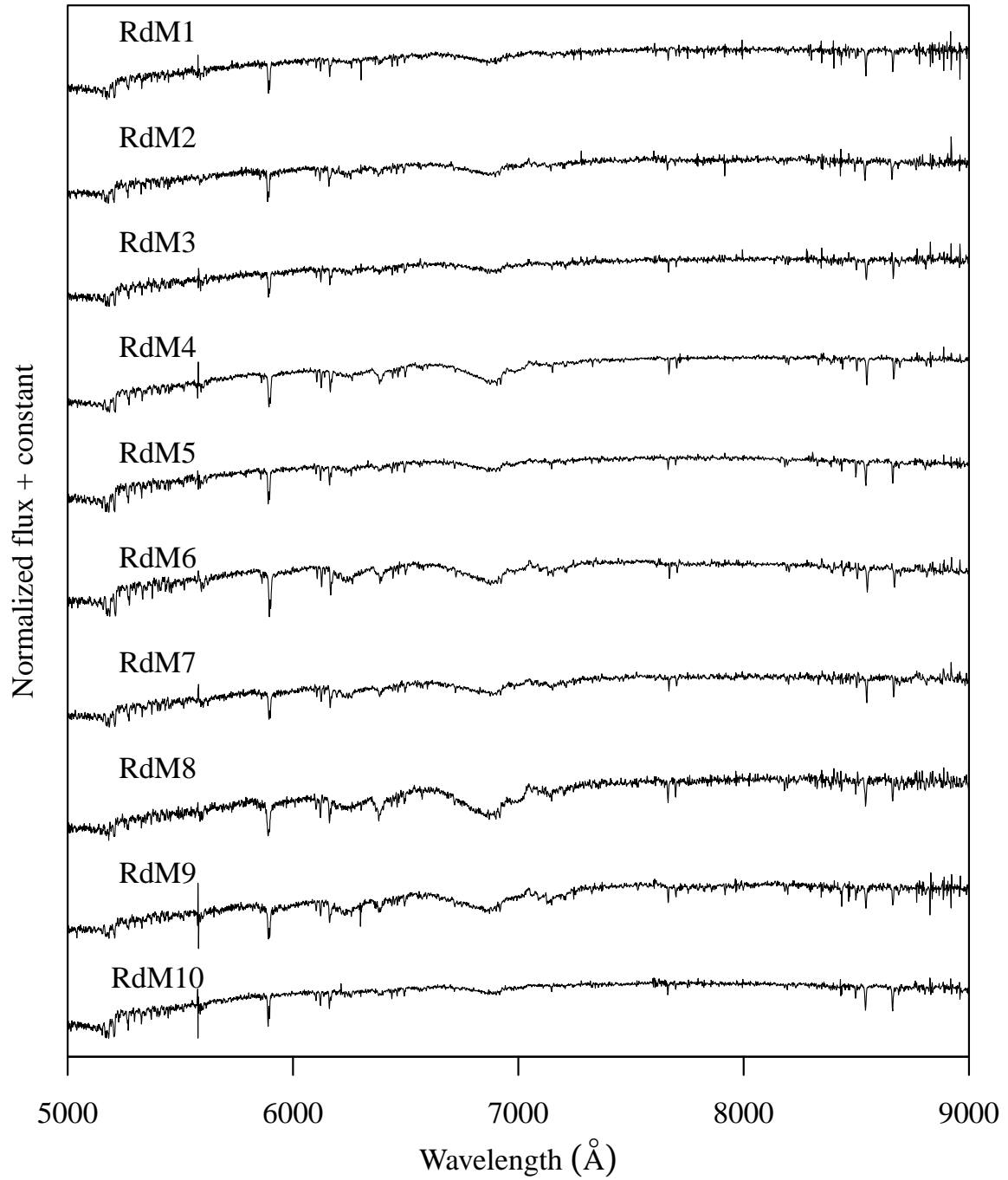


Figure 3. Spectra of our runaway M dwarf candidates. The spectra have been normalized and multiplied by a constant. Another constant has been added to each plot to stack spectra accordingly. Our RdMs show clear TiO and Na features, particularly the 3s→3p Na doublet, in their spectra. The feature at ~ 5600 Å is due to the dichroic cutoff of the red and blue cameras and is not real (Sako et al. 2005; Morgan et al. 2012).

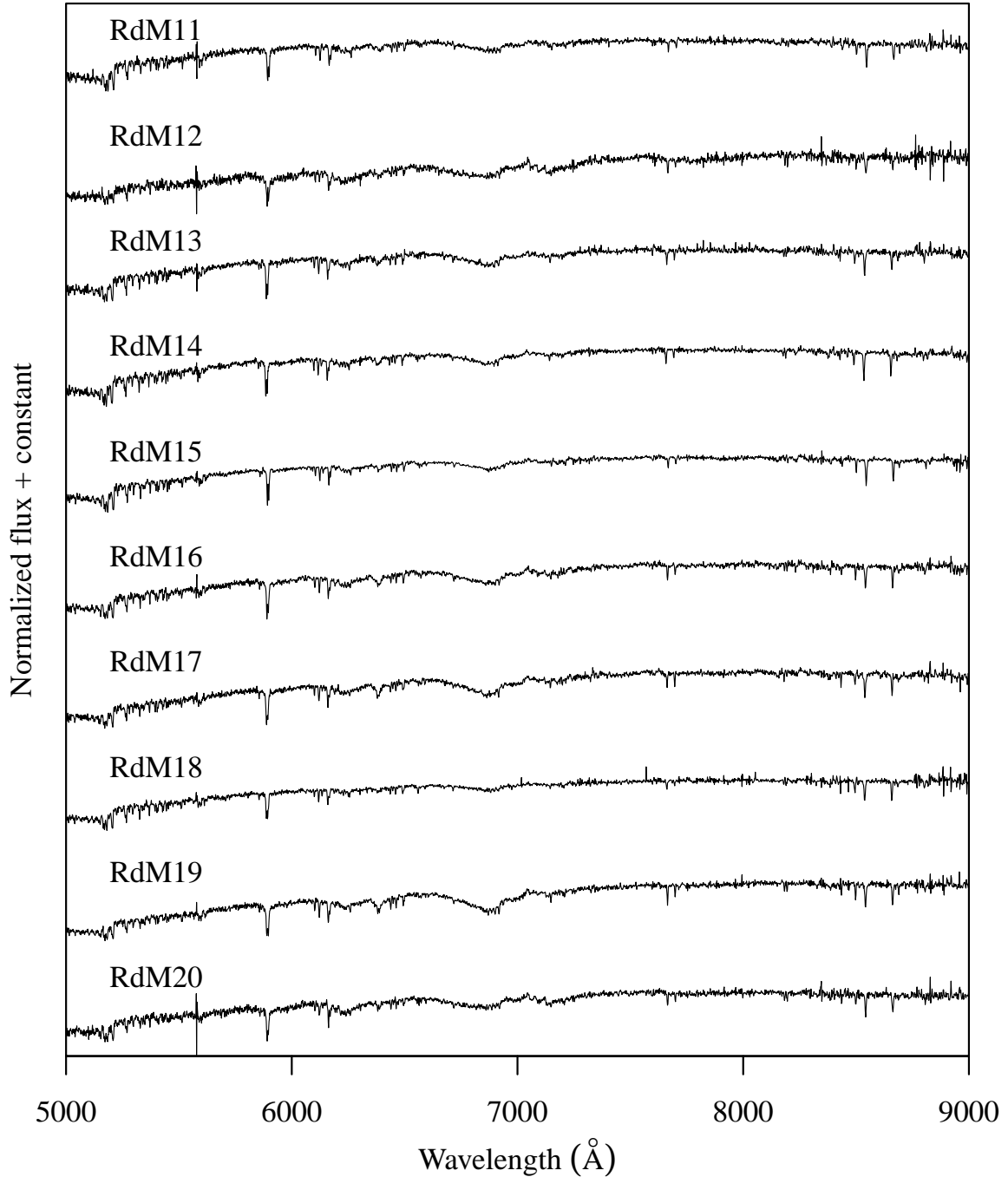

Figure 3. Continued.

Table 4
 Adopted Parameters of the Galactic Potential

M_b (M_\odot)	a_b (kpc)	M_d (M_\odot)	a_d (kpc)	b_d (kpc)	M_h (M_\odot)	r_s (kpc)
3.76	0.1	6×10^{10}	2.75	0.3	10^{12}	20

3.3. Simulations

Table 5 shows that at least two RdMs are unbound, as at their current positions and velocities, they will reach the Galactic virial radius within 1 Gyr. To examine the extent that the position and velocity affect

the candidacy of each RdM as bound or unbound, we performed Monte Carlo simulations with 1000 realizations for each of the RdMs. The results of our simulations depend on the velocity error distribution, of which proper motion errors contribute most significantly. The proper motion error distribution of Dong et al. (2011), which is based on observations of quasars, is modeled by a Gaussian core plus a wing function. According to Figure 3 from Dong et al. (2011), the discrepancy between the normalized core+wing distribution and a normalized core (exclusively) for proper motions within 10 mas yr^{-1} decreases for fainter sources down to $g \leq 20.5$. Since our RdMs have 1σ proper motions errors

Table 5
Galactic Potential Test Results for our Runaway M Dwarf Candidates

RdM	Name	U (km s ⁻¹)	V (km s ⁻¹)	W (km s ⁻¹)	Reaches R_{vir} ?	t_{esc} or $[R_{\text{max}}]^a$ (Myr or [kpc])	Unbound ^b (%)
1	J003012.87-184446.9	646.0 ± 143.0	-374.9 ± 185.3	-24.8 ± 36.5	yes	628.4	77.2
2	J023510.64+004924.9	440.5 ± 115.2	-616.9 ± 179.3	-158.5 ± 112.7	yes	854.0	65.0
3	J035310.50-004928.1	201.4 ± 121.0	-603.4 ± 183.3	-100.2 ± 120.5	no	[44.0]	23.4
4	J100557.07+344549.0	-370.9 ± 126.5	-430.8 ± 113.8	-208.1 ± 94.5	no	[63.5]	24.4
5	J110252.68+274203.7	337.4 ± 73.7	-484.6 ± 176.1	-35.4 ± 19.3	no	[40.5]	11.0
6	J111825.99+090229.4	-422.4 ± 154.7	-466.0 ± 83.9	-110.9 ± 65.9	no	[80.1]	32.3
7	J120525.80+403509.8	-373.2 ± 124.6	-469.3 ± 88.5	41.8 ± 29.5	no	[49.9]	14.8
8	J121441.21+414924.8	-254.8 ± 164.3	-723.8 ± 154.3	-45.5 ± 44.8	no	[146.6]	43.6
9	J131702.01+382435.2	-533.7 ± 122.2	-350.7 ± 88.8	7.2 ± 19.9	no	[156.9]	43.6
10	J140921.10+370542.6	-238.2 ± 178.9	-644.7 ± 165.4	130.1 ± 69.6	no	[72.0]	36.4
11	J142546.68+082717.2	338.0 ± 73.7	-629.2 ± 97.4	-84.5 ± 44.0	no	[100.7]	28.0
12	J153737.72-005608.7	-106.0 ± 19.0	149.5 ± 28.9	96.3 ± 19.0	no	[39.4]	0.0
13	J182547.07+641355.5	-533.9 ± 153.8	-159.9 ± 30.1	-182.8 ± 48.8	yes	1368.9	49.8
14	J184314.08+412258.9	-393.9 ± 91.3	-257.5 ± 27.7	165.1 ± 50.0	no	[44.8]	6.7
15	J203803.39+145300.2	485.6 ± 76.9	-259.4 ± 60.9	-70.7 ± 74.3	no	[69.9]	13.7
16	J221152.95+002207.7	431.0 ± 84.4	-386.0 ± 103.9	-48.4 ± 73.5	no	[53.2]	9.8
17	J224403.71+231532.4	-487.0 ± 91.3	-314.0 ± 28.6	-243.1 ± 51.3	no	[173.6]	41.3
18	J231405.61+230120.2	-434.1 ± 124.5	-304.1 ± 49.3	-27.1 ± 54.3	no	[50.3]	14.3
19	J232541.30+000419.6	-366.6 ± 61.1	-312.8 ± 29.1	-147.9 ± 24.7	no	[36.7]	0.2
20	J235459.63-004133.2	371.4 ± 16.6	-60.8 ± 13.6	20.0 ± 9.1	no	[40.4]	0.0

^a The escape time (t_{esc}) is reported for unbound RdMs, whereas the maximum distance (R_{max}) is reported for bound RdMs. See Section 3.2 for further information.

^b “% Unbound” represents the percentage of our simulations (described in Section 3.3) in which the RdM reaches R_{max} .

within ~ 3 mas yr⁻¹, we have simply adopted a Gaussian distribution of the SDSS+USNO-B proper motion uncertainties for our analysis. The column in Table 5 titled “Unbound” represents the percentage of our simulations in which the RdM reaches R_{max} .

Table 5 shows that RdMs with GC velocities under 570 km s⁻¹, are bound in >50% of our simulations. All but three bound RdMs are expected to turn around within 100 kpc of the Galactic center. About half of our simulations show RdM candidate 13, with GC velocity 571.5 ± 164.1 km s⁻¹, as being bound to the Galaxy. For our hypervelocity candidates, Candidate 1, with GC velocity 658.5 ± 236.9 km s⁻¹, is unbound in 77% of our simulations. We suggest that this RdM may be a true hypervelocity star with over 1σ confidence. Candidate 2 may also be potentially unbound, although we cannot claim much more than $\sim 1\sigma$ confidence due to our high uncertainties, of which proper motion and metallicity uncertainty contribute the most significantly.

4. DISCUSSION

4.1. Selection Effects

We have presented a sample of 20 RdMs which consists primarily of bound tangential velocity outliers and three likely hypervelocity candidates above 1σ confidence. In Section 2.3, we outlined a process by which we created a reduced sample of 192 candidate RdMs prior to examination of their spectra and proper motions. Section 2.4 describes the second stage of the reduction process, in which we examined the spectra of the RdMs by eye. Section 2.5 describes the third and final stage of the reduction process in which we compared the proper motions of the RdMs among multiple catalogs.

Table 6 summarizes the number of dwarfs in each spectral type at each stage of the reduction process. Most of the later-type RdMs were removed from our sample after the first stage as they tended to have noisy spectra and/or large RV errors. We coincidentally ended

Table 6
Number of Dwarfs in Each Spectral Type at Various Reduction Stages

	Stage 1 ^a	Stage 2 ^b	Stage 3 ^c
M0	62	16	16
M1	50	5	4
M2	18	0	0
M3	21	0	0
M4	19	0	0
M5	11	2	0
M6	6	1	0
M7	5	0	0

^a 192 RdM candidates, Section 2.3

^b 24 RdM candidates, Section 2.4

^c 20 RdM candidates, Section 2.5

up omitting the M5 and M6 candidates due to mismatched proper motions between SDSS+USNO-B and WISE+SDSS+2MASS. Our selection process does not necessarily mean that all later-type (>M4) dMs have bad spectra. Out of the $\sim 2 \times 10^4$ later-type dMs in W11, ~ 1600 have GC velocities exceeding 400 km s⁻¹. Initial U, V, W velocities come from proper motions taken from Munn et al. (2004), which are also biased toward earlier-type dMs.

To test whether the process of flagging stars with bad spectra or Na shifts biased the kinematics of our sample, we performed independent one-way ANOVA tests for each of U, V, W between our initial sample of 192 RdMs and our final sample of 20 RdMs. Table 7 presents the results of our ANOVA tests, where SD represents the standard deviation, df is the number of residual degrees of freedom, F is the F -ratio, and p is the p -value. We mark statistically significant p -values < 0.05 with an asterisk. Table 7 shows that there is no statistically significant difference in the U or W kinematics between the two samples; however, the final sample has a significantly lower $\langle V \rangle$ than the initial sample ($\langle V \rangle = -385.0$ km s⁻¹ com-

Table 7
ANOVA Test of Sample Kinematics

	n	M (km s $^{-1}$)	SD (km s $^{-1}$)	df	F	p
U	192	-49.8	486	210	0.01	0.91
	20	-63.2	412.5			
V	192	-57.1	444.2	210	10.61	< 0.05*
	20	-385.0	212.8			
W	192	203.9	703.4	210	2.62	0.11
	20	-51.4	109.4			

Statistically significant p -values are marked with an asterisk.

pared to $\langle V \rangle = -57.1$ km s $^{-1}$). A similarly negative $\langle V \rangle$ for subdwarf RdMs has been previously observed (see Table 7 of Savcheva et al. 2014, $\langle V \rangle = -458.3$ km s $^{-1}$). Negative V velocities are consistent with asymmetric drift and dynamical interactions. We do not see any obvious reason for why our selection process, based on inspection of their spectra by eye and comparison thereafter of their proper motions, would significantly offset the V kinematics of our final sample.

We thus ask whether or not we should expect to observe an isotropic M dwarf stellar velocity distribution near the Solar neighborhood. If so, then the TV should be $\sqrt{2}$ times larger than the RV. Figure 4 shows that our sample of 20 RdMs tends toward higher TVs than RVs. Palladino et al. (2014a) noted that their sample of 20 G and K dwarfs suffered from a high TV to RV ratio (see Figure 1 in the erratum Palladino et al. 2014b), which they suggest is the result of possible contamination due to large proper motion errors. Their Monte Carlo analysis adopts the proper motion error distribution of Dong et al. (2011), which models the proper motion errors of quasars by a Gaussian core plus a wing function. The analysis by Palladino et al. (2014a) revealed that 13 of their 20 G and K dwarfs retain hypervelocity status, and all of their candidates have less than a 25% probability of being interlopers. In Table 2, we checked that the proper motions of our sample are generally consistent among multiple catalogs to within the uncertainties, so we suggest that the likelihood of contamination due to proper motion errors in our sample is minimal.

Since the SDSS footprint is largely out of the Galactic plane, we expect the W velocity should trace the RVs. Our mean W and RV sample velocities are -54.8 km s $^{-1}$ and -65.1 km s $^{-1}$, respectively, which thus suggests an overall low RV contribution to the total velocity. Kenyon et al. (2014) compared their simulated distance-limited proper motion and RV distributions for hypervelocity stars and runaway stars in the range $1 - 3 M_{\odot}$ for both supernova and dynamical ejection scenarios. Kenyon et al. (2014) found that while the RVs initially published by Palladino et al. (2014a) are consistent with their model predictions, the large proper motions are not. Using improved proper motion measurements for 14 of the 20 stars based on all available images including SDSS at different epochs, Ziegerer et al. (2015) showed that 11 of these 14 stars are bound in over 99% of their simulations. Ziegerer et al. (2015) concluded that 13 stars belong to the disk population and have kinematics consistent with a binary supernova or perhaps a disk runaway mechanism (Kenyon et al. 2014), while the remaining star may belong to the halo. The models developed by Kenyon et al. (2014), however, have a lower mass limit of $1 M_{\odot}$,

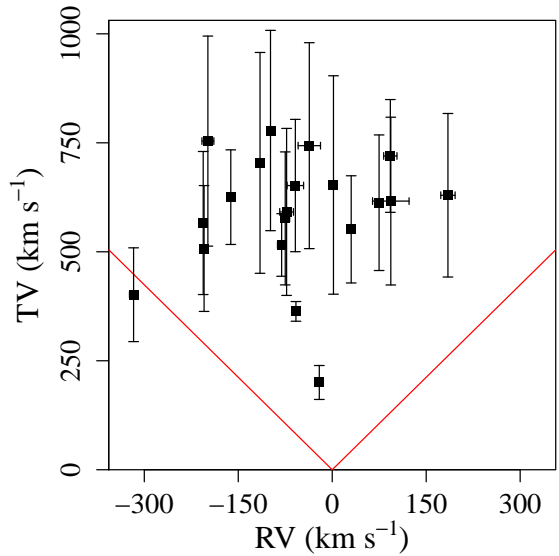


Figure 4. Tangential vs. radial velocities of our RdM sample, with 1σ error bars. The red lines correspond to a perfectly isotropic velocity distribution, where the tangential velocity is $\sqrt{2}$ times larger than the radial velocity. As in Figure 1 of Palladino et al. (2014b), the majority of our sample has much higher tangential velocities than radial velocities. Our proper motion comparisons, in Table 2, however, suggest that our sample is not contaminated by high proper motion errors.

and so their predicted velocity distributions may not be reliably applied to the lowest mass M dwarfs, $\sim 0.1 M_{\odot}$, which are the dominant stellar constituent.

4.2. Tangential Velocities

One initial observation of the stellar kinematics in Table 7 is that the W velocity dispersion, 109.4 km s $^{-1}$, is much lower than the U and V velocity dispersions, at 486.0 km s $^{-1}$ and 444.2 km s $^{-1}$, respectively. The SDSS footprint is largely out of the Galactic plane (York et al. 2000), so we should expect a low W dispersion to be associated with a small RV dispersion. If we compare the absolute values of W and RV over the sample, then we calculate a total W to RV ratio of 0.89. Likewise, if we compare the absolute values of U , V , and TV over the sample, then we compute a total U to TV ratio of 0.66 and a total V to TV ratio of 0.68.

To assess whether the tangential velocities suffer large systematic errors, we compare the kinematic dispersion with that of 14 M subdwarfs with GC velocities exceeding 525 km s $^{-1}$, published in Savcheva et al. (2014), and the G and K dwarf sample, published in Palladino et al. (2014a) and Ziegerer et al. (2015). The velocity dispersions $\sigma_U, \sigma_V, \sigma_W$ in Savcheva et al. (2014) are 381 km s $^{-1}$, 283 km s $^{-1}$, and 191 km s $^{-1}$, respectively, which suggests that a low velocity dispersion in the W component is not unique to our study. Moreover, Savcheva et al. (2014) observed lower W velocity dispersions than U or V velocity dispersions for each M subdwarf metallicity class in their sample, as well as for non-hypervelocity stars in their sample (Bochanski et al. 2013). Fuchs et al. (2009) observed a similar trend for M dwarfs in the thin disk from SDSS DR7.

For comparison with the study of Palladino et al. (2014a), Palladino et al. (2014a) used only SDSS photometry, whereas Ziegerer et al. (2015) derived new proper motions for 14 of 20 stars “by combining all

astrometric information at hand from digitized plates and modern surveys.” Their published proper motions give velocity dispersions $\sigma_U, \sigma_V, \sigma_W$ of 59.5 km s^{-1} , 43.6 km s^{-1} , and 91.6 km s^{-1} , respectively. The low radial velocities of their sample are consistent with a low W velocity dispersion. The observed U and V velocity dispersions observed by Ziegerer et al. (2015) are lower than the W velocity dispersion.

Why does Savcheva et al. (2014) find *lower* W velocity dispersions than U or V velocity dispersions, when Ziegerer et al. (2015) find the opposite? The answer may lie in the sampled kinematics of the stars. The mean Galactocentric velocity of the 14 stars under consideration in Ziegerer et al. (2015) is 282 km s^{-1} , and only 3 stars retain Galactocentric velocities exceeding 400 km s^{-1} . The 14 M subdwarfs with published in Savcheva et al. (2014) have a mean Galactocentric velocity of 674 km s^{-1} , which is along the tail end of stellar kinematic models involving supernova ejections and dynamical interactions (Kenyon et al. 2014, and references therein). Our proper motions are confirmed by other catalogs (Table 2), and while our distance uncertainties are larger, they cannot account for the high tangential motions that we observe. Since the mean Galactocentric velocity of our RdM sample is 486 km s^{-1} , it is perhaps to be expected that our velocity dispersions are not in agreement with those observed by Ziegerer et al. (2015).

Sellwood and Binney (2002) identified a mechanism that explains the radial migration of stars due to exchanges in angular momentum caused by transient spiral modes. In these modes, transient spiral arms can move corotating stars without heating the disk. These modes are consistent with a break in the stellar surface density that propagates radially outward within the disk Roškar et al. (2008). Vera-Ciro et al. (2014) simulated the evolution of a galaxy representative of the Milky Way and the effect of the spiral modes on the stellar velocity dispersion. Our M dwarfs have systematically negative V velocities, so a 5 Gyr evolution, as simulated by Vera-Ciro et al. (2014), might be a long enough time for perturbations due to spiral arm torques to perturb the orbits of these stars so that they lag behind the rest of the disk. Figure 5 of Vera-Ciro et al. (2014) show that the Galactocentric radial and azimuthal velocity dispersions, which represent σ_U and σ_V at the location of the Sun, naturally increase $\sim 30\%$ more than the vertical velocity dispersion, σ_W . The increase interestingly seems to peak particularly near the Galactocentric radius of the Sun of $\sim 8 \text{ kpc}$. The higher σ_U, σ_V compared to σ_W is consistent with the kinematics of our RdM sample and of the hypervelocity star sample published in Savcheva et al. (2014).

Dynamical heating has been alternatively suggested a source for M dwarf disk runaways (West et al. 2008; Savcheva et al. 2014). In particular, Savcheva et al. (2014) examined the 3D velocities of field M dwarfs from W11 and 3517 new subdwarfs and argued that thin-disk dynamical heating may cause the older stars to have highly elliptical Galactic orbits that take them out of the disk. These orbits would allow for higher observed velocity dispersions in the solar neighborhood. Simulations of dynamical heating predict typical W dispersions of $\lesssim 20 \text{ km s}^{-1}$ for M dwarfs (see Figure 6 of West et al.

2006 and Figure 5 of West et al. 2008). However, these studies do not target hypervelocity star candidates, and so we do not quantify whether such models may be generalized to explain the high velocity dispersions in our sample.

4.3. Speculation of Origins

To examine the extent to which the RdMs share a GC origin, we calculate the absolute difference in the angle between the GC position vector in the X, Y, Z coordinate system and the GC velocity vector, v_{tot} (defined in Section 3.1). In Figure 5, we plot, for each RdM, the absolute difference (axis label $|\Delta\theta|$) between the GC position angle and v_{tot} , with 1σ error bars calculated using the procedure in Appendix B. The values $\Delta\theta = 0^\circ$ ($\Delta\theta = 180^\circ$) represent motion directly radially out from (in toward) the Galactic center. The value $\Delta\theta = 90^\circ$ represents circular motion around the Galactic center. Our RdMs, which are all within $\sim 1 \text{ kpc}$ of the Sun, tend not to exhibit circular motion around the Galactic center, as exhibited by the absence of RdMs with $\Delta\theta = 90^\circ$.

Figure 5 presents a case against a GC origin for about half of our RdMs. The range of possible differences in GC position angle and GC velocity angle rules out the values 0° (radially outward from the Galactic center) and 180° (radially inward toward the Galactic center) to within 1σ for 12 RdMs and 2σ for 8 RdMs. Hence, only about half of our RdMs have kinematics consistent with a GC origin. We note that some RdMs may not actually reach the Galactic virial radius and instead have turned around. Interestingly, RdMs 1 and 2, which have an inward velocity component, are likely unbound, as established in Table 5, yet they are getting *closer* to the Galactic center. Such an observed velocity is inconsistent with an ejection mechanism from the center of the Milky Way, and so the origin of their high tangential velocities is unlikely to be Galactocentric. Other acceleration mechanisms, the origins of which we describe below, may influence an otherwise exclusive GC origin.

One possible alternate ejection mechanism is through a supernova explosion (Tauris 2015, and references therein), as the energy of the ejection could push the companion star forward. In the supernova ejection scenario pertaining to G and K stars, Tauris (2015) showed that GC velocities up to ~ 770 and $\sim 1280 \text{ km s}^{-1}$ are possible for these stars, respectively. Such an explosion would also contribute metals to the companion star. As 16 of our 20 RdMs have $\zeta > 0.825$ (they are dwarfs, rather than a type of subdwarf), we cannot rule out the possibility that one or more of our RdMs may have been accelerated from a supernova. Since abundance measurements for dMs are uncertain to $\sim 0.2 \text{ dex}$, we do not have any way to probe if the RdMs are being enriched given current abundance measurements.

Another plausible mechanism for accelerating main-sequence stars is dynamic ejection through multi-body interactions. Kollmeier et al. (2009) initially determined a maximum ejection rate of 35 Myr^{-1} for old population stars from the Galactic center. Using a Solar-neighborhood survey volume of 265 kpc^3 , Kollmeier et al. (2010) found that ejection rates are even lower for late-type stars and stars with sub-solar metallicities. Our RdM sample is systematically metal-rich and so is

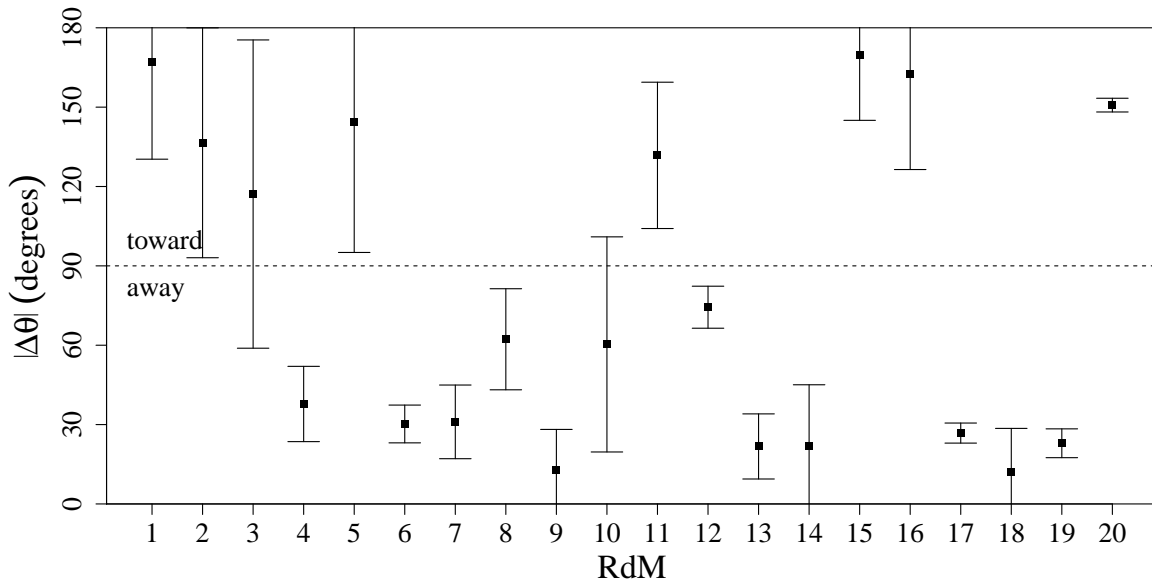


Figure 5. Absolute difference between the GC position angle and v_{tot} (vertical axis, $|\Delta\theta|$), for each RdM, with 1σ error bars. RdMs with $|\Delta\theta| < 90^\circ$ are moving away from the Galactic center, whereas RdMs with $|\Delta\theta| > 90^\circ$ are moving towards the Galactic center. About half of our RdMs have kinematics that are not consistent with a strictly radial origin out away from, or toward, the Galactic center. RdMs 2, 4, and 14 are expected to leave the Galaxy, but are currently getting closer to the Galactic center, which suggests that they may not have been ejected out of the center of the Milky Way.

at least consistent with the results of Kollmeier et al. (2010). Gvaramadze & Gualandris (2011) simulated the effect of a three-body system consisting of two high mass ($\geq 80 M_\odot$) stars and a flyby star in the mass range 3–80 M_\odot . According to their simulations (see Figure 4 and Figure 9 of Gvaramadze & Gualandris 2011), about 1% (10%) of simulations for each of the stars with masses $\lesssim 20 M_\odot$ had escape velocities exceeding 400 km s^{-1} (200 km s^{-1}).

Because these simulations include only very high mass stars, which are short-lived and comprise a tiny fraction of the stellar population, the actual probability of observing such a high escape velocity due to interacting contact binaries is low. Perets & Šubr. (2012) modeled the rate of high-velocity runaways from binaries in dense, compact clusters or cluster cores, with primary star masses $\geq 4 M_\odot$. Perets & Šubr. (2012) showed that the ejection rate of hyper-runaways from binaries in dense, compact clusters or cluster cores is on the order of 10–20 stars per 100 Myr, of which only one or two such stars have $v_{\text{esc}} > 400 \text{ km s}^{-1}$. Our survey volume covers about one quarter of the sky out to 1 kpc. On the basis of these analyses, it is statistically unlikely that our RdMs were accelerated to potentially hypervelocity speeds through a dynamic ejection mechanism. The kinematics of our sample, as illustrated in Figure 2 and Figure 5, nonetheless show that high TVs dominate the kinematics of the majority of our RdMs.

A third plausible mechanism for generating high tangential velocities is through accelerations from nearby galaxies. Li et al. (2012) proposed that some hypervelocity stars may be accelerated through tidal disruptions of the Milky Way’s dwarf galaxies or gravitational interactions with the CMBH of M31 or M32. We briefly consider how plausible these alternative mechanisms may explain the origins of our RdMs. Lu et al. (2007) and Sherwin et al. (2008) respectively proposed that some hypervelocity stars may be ejected out of M32 and M31, with higher

ejection rates out of M32. The predicted space density of M31 hypervelocity stars of all types near the Sun is $\sim 0.001 \text{ kpc}^3$. Given our survey volume, the probability of discovering a single M31 hypervelocity star, based on its predicted space density near the Sun, is low ($\sim 0.1\%$). For comparison, we observed 20 RdMs within our survey volume, so to first order, the probability of any of our RdMs coming from M31 is $1 - (1 - 0.004)^{20}$, or $\sim 8\%$. In addition, Abadi et al. (2009) suggested that the disruption of tidal dwarf galaxies in the Milky Way could have produced the stream of hypervelocity stars in the constellation Leo ($l \approx 230^\circ$, $b \approx 60^\circ$).

We quantify whether or not our RdMs may have originated from the direction of M31 or the Leo stream. We arrive at formulas for the uncertainty in the Galactic latitude b and Galactic longitude l of the velocity angle using the procedure in Appendix C. Table 8 presents the differences and 2σ uncertainties between each RdM velocity direction, in Galactic coordinates, and the direction of M31 and the Leo stream. According to Sherwin et al. (2008), for the purpose of analyzing hypervelocity stars, one may reasonably “assume a static configuration over the last 10^{10} yr, with M31 and the [Milky Way] separated by their current distance.” In Table 8, $\Delta\psi$ is the difference between the angle of the source (M31 or Leo) and the RdM velocity angle. The value $\Delta\psi = 180^\circ$ represents a star whose velocity angle is opposite the position angle of the source; that is, the star came from that source, assuming a constant flight path. The uncertainty in $\Delta\psi_{\text{source}}$ is the uncertainty in the RdM velocity angle, $\sigma_{\theta,v}$, which we calculate using the procedure in Appendix B.

Table 8 shows that seven RdMs have velocity angles that point opposite the position of M31 to within 2σ . RdMs 1 and 2, with GC velocities of 659 km s^{-1} and 595 km s^{-1} , respectively, are likely unbound, as analyzed in Section 3.2. Assuming constant GC velocity and a distance of 800 kpc to M31, the flight times of these stars

Table 8
RdM Velocity Angles and Position Angles of M31 and Leo Stream

RdM	Name	b (deg.) ^a	l (deg.) ^a	$\Delta\psi_{\text{M31}}$ (deg.) ^{a,b}	$\Delta\psi_{\text{Leo}}$ (deg.) ^{a,c}
1	J003012.87-184446.9	-2.2 ± 13.5	349.1 ± 72.1	127.5 ± 73.2	106.0 ± 73.2
2	J023510.64+004924.9	-15.5 ± 37.3	320.2 ± 81.1	138.5 ± 86.7	103.4 ± 86.7
3	J035310.50-004928.1	-13.8 ± 50.6	299.7 ± 107.4	144.6 ± 116.4	92.2 ± 116.4
4	J100557.07+344549.0	-26.8 ± 7.0	206.0 ± 30.6	76.1 ± 28.4	89.0 ± 28.4
5	J110252.68+274203.7	-4.9 ± 8.3	325.2 ± 98.4	144.6 ± 98.4	96.9 ± 98.4
6	J111825.99+090229.4	-13.2 ± 13.3	207.1 ± 2.4	81.5 ± 13.5	75.4 ± 13.5
7	J120525.80+403509.8	5.5 ± 26.1	210.4 ± 7.9	91.3 ± 27.2	56.5 ± 27.2
8	J121441.21+414924.8	-4.8 ± 13.4	241.7 ± 35.8	116.1 ± 38.2	65.5 ± 38.2
9	J131702.01+382435.2	0.8 ± 9.7	190.7 ± 28.9	71.3 ± 30.5	66.5 ± 30.5
10	J140921.10+370542.6	15.8 ± 70.4	238.9 ± 44.3	121.1 ± 80.9	44.7 ± 80.9
11	J142546.68+082717.2	-9.4 ± 17.3	311.7 ± 53.2	147.3 ± 55.2	94.1 ± 55.2
12	J153737.72-005608.7	13.1 ± 7.2	104.9 ± 14.3	38.2 ± 15.7	94.8 ± 15.7
13	J182547.07+641355.5	-18.7 ± 0.1	170.4 ± 25.1	46.1 ± 23.8	92.1 ± 23.8
14	J184314.08+412258.9	22.7 ± 44.1	181.1 ± 16.0	73.3 ± 46.4	50.4 ± 46.4
15	J203803.39+145300.2	-8.3 ± 39.3	358.9 ± 30.0	116.0 ± 49.1	115.8 ± 49.1
16	J221152.95+002207.7	-6.1 ± 37.8	342.5 ± 62.2	130.9 ± 72.2	106.4 ± 72.2
17	J224403.71+231532.4	-26.3 ± 1.9	187.5 ± 8.0	60.1 ± 7.4	93.1 ± 7.4
18	J231405.61+230120.2	-3.5 ± 26.3	187.1 ± 19.2	66.3 ± 32.6	71.8 ± 32.6
19	J232541.30+000419.6	-21.7 ± 0.6	189.7 ± 11.7	63.1 ± 10.9	88.0 ± 10.9
20	J235459.63-004133.2	2.7 ± 4.4	27.0 ± 2.5	94.9 ± 5.1	114.7 ± 5.1

^a Uncertainties are 2σ .

^b M31 is located at $b = -21.573^\circ$, $l = 121.174^\circ$.

^c The Leo stream is located at approximately $b = +60^\circ$, $l = 230^\circ$.

are approximately 1.2 Gyr and 1.3 Gyr, respectively. Table 8 also shows that four RdMs have velocity angles that point along the direction of the Leo stream to within 2σ , which suggests that no more than four RdMs could have originated from the Leo stream.

5. SUMMARY

We have presented a sample of 20 runaway M dwarf candidates (RdMs) with Galactocentric (GC) velocities exceeding 400 km s^{-1} within 1 kpc of the Sun assessed their candidacy for being unbound from the Milky Way. Our sample is taken from the West et al. (2011) catalog. We corrected for extinction using the method of Jones et al. (2011), or, if the star was not present in that catalog, the method of Schlegel et al. (1998). We updated the catalog distances by correcting for the effect of metallicity using the method of Bochanski et al. (2013). Our RdMs pass a series of photometric and proper motion processing flags to minimize contamination. To ensure that our sample contained high-quality SDSS spectra, we inspected the optical spectra of each RdM by eye and flagged stars with noisy spectra or sodium shifts inconsistent with their measured radial velocities.

To ensure that our final sample was not contaminated by high proper motion errors, we compared the proper motions of the remaining RdMs among multiple catalogs, including SDSS+USNO-B (used in West et al. 2011), PP-MXL (Roeser et al. 2010), the Lépine Shara Proper Motion catalog (LSPM, Lépine & Shara 2005), and a master catalog combining data from the *Wide-field Infrared Survey Explorer* (*WISE*, Wright et al. 2010), SDSS, and the Two-Micron All-Sky Survey (2MASS), the analysis of which is being conducted separately (Theissen et al., submitted). We flagged stars whose proper motions in West et al. (2011) were inconsistent with those of the other catalogs. In total, we retained 20 stars from the original catalog of West et al. (2011)

To determine if each RdM is unbound, we modeled the Galactic potential using a bulge-disk-halo profile

(Kenyon et al. 2008; Brown et al. 2014). We found that five of our RdMs are expected to reach the Galactic virial radius. Our fastest RdM, with Galactocentric velocity $658.5 \pm 236.9 \text{ km s}^{-1}$, is a possible hypervelocity candidate, as it is unbound in 77% of our simulations. The majority of our RdMs are likely disk runaways or halo objects. Hence, our study thus provides some confidence in the possible discovery of one hypervelocity M dwarf. About half of our RdMs have kinematics consistent with an ejection scenario from M31 or M32 to within 2σ , although our distance-limited survey makes such a realization unlikely. No more than four of our RdMs may have originated from the Leo stream. We instead propose that a series of multi-body interactions within the Galactic disk and/or accelerations from supernovae are plausible alternative mechanisms. If *Gaia*³ meets its predicted astrometric performance, which would yield proper motion uncertainties of $0.035\text{--}0.17 \text{ mas yr}^{-1}$, then it should unambiguously determine whether or not our fastest RdM is indeed a hypervelocity star. The growing number of low-mass tangential velocity outliers, such as those in this study and in Ziegerer et al. (2015), will also be of great interest in the *Gaia* era for investigating their possible origins.

We would like to thank the anonymous referee for his/her comments, which significantly improved the quality of our revised manuscript. The authors would like to acknowledge John J. Bochanski for kindly providing us with the parameters for the M subdwarf color-magnitude relations in Bochanski et al. (2013).

A.A.W. acknowledges funding from NSF grants AST-1109273 and AST-1255568. C.A.T. would like to acknowledge the Ford Foundation for financial support. A.A.W. and C.A.T. also acknowledge the support of the Research Corporation for Science Advancement's Cot-

³ <http://www.cosmos.esa.int/web/gaia/science-performance>

trell Scholarship.

Funding for SDSS-III has been provided by the Alfred P. Sloan Foundation, the Participating Institutions, the National Science Foundation, and the U.S. Department of Energy Office of Science. The SDSS-III web site is <http://www.sdss3.org/>.

SDSS-III is managed by the Astrophysical Research Consortium for the Participating Institutions of the SDSS-III Collaboration including the University of Arizona, the Brazilian Participation Group, Brookhaven National Laboratory, Carnegie Mellon University, University of Florida, the French Participation Group, the German Participation Group, Harvard University, the Instituto de Astrofísica de Canarias, the Michigan State/Notre Dame/JINA Participation Group, Johns Hopkins University, Lawrence Berkeley National Laboratory, Max Planck Institute for Astrophysics, Max Planck Institute for Extraterrestrial Physics, New Mexico State University, New York University, Ohio State University, Pennsylvania State University, University of Portsmouth, Princeton University, the Spanish Participation Group, University of Tokyo, University of Utah, Vanderbilt University, University of Virginia, University of Washington,

and Yale University.

This publication makes use of data products from the Two Micron All Sky Survey, which is a joint project of the University of Massachusetts and the Infrared Processing and Analysis Center/California Institute of Technology, funded by the National Aeronautics and Space Administration and the National Science Foundation.

This publication also makes use of data products from the *Wide-field Infrared Survey Explorer*, which is a joint project of the University of California, Los Angeles, and the Jet Propulsion Laboratory/California Institute of Technology, funded by the National Aeronautics and Space Administration.

This research made use of R, a language and environment for statistical computing and graphics. Analyses and figures in this work were created using R. The FITSio package, which we used to examine SDSS spectra by eye, was developed by Andrew Harris. The Hmisc package was developed by Charles Geyer, University of Chicago, and modified by Frank Harrell, Vanderbilt University. The R website is <http://www.R-project.org>.

APPENDIX

A. SODIUM TRANSITIONS

Table 9
Rest Frame Sodium Transitions in Vacuum

Transition	λ_{vac} (Å)
3s→3p doublet	5891.58
	5897.56
3p→3d triplet	8185.51
	8197.05
	8197.08

B. UNCERTAINTY IN THE ANGLE BETWEEN THE GALACTOCENTRIC POSITION AND GALACTOCENTRIC VELOCITY

Consider a star located at GC position \mathbf{r} moving with Galactic rest frame velocity \mathbf{v} measured at the location of the star. The uncertainty in \mathbf{r} depends on σ_X , σ_Y , σ_Z , which are the uncertainties in X , Y , Z , respectively. Let \mathbf{r}_+ and \mathbf{r}_- represent the maximum and minimum GC positions, respectively, so that

$$\mathbf{r}_{\pm} = (X \pm \sigma_X)\mathbf{X} + (Y \pm \sigma_Y)\mathbf{Y} + (Z \pm \sigma_Z)\mathbf{Z}. \quad (\text{B1})$$

The angle between \mathbf{r}_+ and \mathbf{r}_- is determined by

$$\cos(\sigma_{\theta,\mathbf{r}}) = \frac{\mathbf{r}_+ \cdot \mathbf{r}_-}{|\mathbf{r}_+||\mathbf{r}_-|}, \quad (\text{B2})$$

where $\sigma_{\theta,\mathbf{r}}$ is the uncertainty in the direction of \mathbf{r} .

Likewise, the uncertainty in \mathbf{v} depends on the uncertainties in each component, where $(dX/dt) = -U$, $(dY/dt) = V + v_{\text{LSR}}$, and $(dZ/dt) = W$. Let \mathbf{v}_+ and \mathbf{v}_- represent the maximum and minimum velocities, respectively, so that

$$\mathbf{v}_{\pm} = -(U \pm \sigma_U)\mathbf{X} + (V + v_{\text{LSR}} \pm \sigma_V)\mathbf{Y} + (W \pm \sigma_W)\mathbf{Z}. \quad (\text{B3})$$

The angle between \mathbf{v}_+ and \mathbf{v}_- is determined by

$$\cos(\sigma_{\theta,\mathbf{v}}) = \frac{\mathbf{v}_+ \cdot \mathbf{v}_-}{|\mathbf{v}_+||\mathbf{v}_-|}, \quad (\text{B4})$$

where $\sigma_{\theta,\mathbf{v}}$ is the uncertainty in the angle of \mathbf{v} . In the limit of small angle approximations, the total uncertainty in the angle between \mathbf{r} and \mathbf{v} , which we denote σ_{θ} , is determined by adding the position and velocity angle uncertainties in quadrature:

$$\sigma_{\theta} = \sqrt{(\sigma_{\theta,\mathbf{r}})^2 + (\sigma_{\theta,\mathbf{v}})^2}. \quad (\text{B5})$$

C. UNCERTAINTY IN THE GALACTIC LATITUDE AND GALACTIC LONGITUDE OF THE VELOCITY ANGLE

Consider a star moving with Galactic rest frame velocity \mathbf{v} . To determine the uncertainty in the Galactic latitude of \mathbf{v} , we project \mathbf{v} onto a plane that measures its speed parallel to the plane and its velocity perpendicular to the plane. This velocity, which we denote \mathbf{v}_b , is given by

$$\mathbf{v}_b = \sqrt{U^2 + (V + v_{\text{LSR}})^2} \boldsymbol{\rho} + W \mathbf{Z}, \quad (\text{C1})$$

where $\boldsymbol{\rho}$ points parallel to the Galactic midplane. The uncertainty in \mathbf{v}_b follows a similar procedure to that in Appendix B. Let \mathbf{v}_{b+} and \mathbf{v}_{b-} represent the maximum and minimum projected velocities, respectively, so that

$$\mathbf{v}_{b\pm} = \sqrt{(U \pm \sigma_U)^2 + (V + v_{\text{LSR}} \pm \sigma_V)^2} \boldsymbol{\rho} + (W \pm \sigma_W) \mathbf{Z}. \quad (\text{C2})$$

The angle between \mathbf{v}_{b+} and \mathbf{v}_{b-} is determined by

$$\cos(\sigma_b) = \frac{\mathbf{v}_{b+} \cdot \mathbf{v}_{b-}}{|\mathbf{v}_{b+}| |\mathbf{v}_{b-}|}, \quad (\text{C3})$$

where σ_b is the uncertainty in the Galactic latitude of \mathbf{v} .

To determine the uncertainty in the Galactic longitude of \mathbf{v} , we project \mathbf{v} directly onto the Galactic plane. This velocity, which we denote \mathbf{v}_l , is given by

$$\mathbf{v}_l = -U \mathbf{X} + (V + v_{\text{LSR}}) \mathbf{Y}. \quad (\text{C4})$$

Let \mathbf{v}_{l+} and \mathbf{v}_{l-} represent the maximum and minimum projected velocities, respectively, so that

$$\mathbf{v}_{l\pm} = -(U \pm \sigma_U) \mathbf{X} + (V + v_{\text{LSR}} \pm \sigma_V) \mathbf{Y}. \quad (\text{C5})$$

The angle between \mathbf{v}_{l+} and \mathbf{v}_{l-} is determined by

$$\cos(\sigma_l) = \frac{\mathbf{v}_{l+} \cdot \mathbf{v}_{l-}}{|\mathbf{v}_{l+}| |\mathbf{v}_{l-}|}, \quad (\text{C6})$$

where σ_l is the uncertainty in the Galactic longitude of \mathbf{v} .

REFERENCES

- Abadi, M. G., Navarro, Julio F., & Steinmetz, M. 2009, *ApJ*, 691, L63
- Abazajian, K. N., Adelman-McCarthy, J. K., Agüeros, M. A., et al. 2009, *ApJS*, 182, 543
Univ. Press).
- Bochanski, J. J., West, A. A., Hawley, S., & Covey, K. 2007, *AJ*, 133, 531
- Bochanski, J. J., Hawley, S. L., Covey, K. R., et al. 2010, *AJ*, 139, 2679
- Bochanski, J. J., Savcheva, A., West, A. A., & Hawley, S. L. 2013, *AJ*, 145, 40
- Bromley, B. C., Kenyon, S. J., Geller, M. J., Barcikowski, E., Brown, W. R., & Kurtz, M. J. 2006, *ApJ*, 653, 1194
- Bromley, B. C., Kenyon, Brown, W. R., & S. J., Geller. 2009, *ApJ*, 706, 925
- Brown, W. R., Geller, M. J., Kenyon, S. J., & Kurtz, M. J. 2005, *ApJ*, 622, L33
- Brown, W. R., Geller, M. J., Kenyon, S. J., & Kurtz, M. J. 2006a, *ApJ*, 640, L35
- Brown, W. R., Geller, M. J., Kenyon, S. J., & Kurtz, M. J. 2006b, *ApJ*, 647, 303
- Brown, W. R., Geller, M. J., Kenyon, S. J., Kurtz, M. J., & Bromley, B. C. 2007a, *ApJ*, 660, 311
- Brown, W. R., Geller, M. J., Kenyon, S. J., Kurtz, M. J., & Bromley, B. C. 2007b, *ApJ*, 671, 1708
- Brown, W. R., Anderson, J., Gnedin, O. Y., et al. 2010, *ApJ*, 719, L23
- Brown, W. R., Geller, M. J., & Kenyon, S. J. 2012, *ApJ*, 751, 55
- Brown, W. R., Geller, M. J., & Kenyon, S. J. 2014, *ApJ*, 787, 89
- Covey, K. R., Ivezić, Ž., Schlegel, D., et al. 2007, *AJ*, 134, 2398
- Dhital, S., West, A. A., Stassun, K. G., et al. 2012, *AJ*, 143, 67
- Dong, R., Gunn, J., Knapp, G., Rockosi, C., & Blanton, M. 2011, *AJ*, 142, 116
- Edelmann, H., Napiwotzki, R., Heber, U., Christlieb, N., & Reimers, D. 2005, *ApJ*, 634, L181
- Fuchs, B., Dettbarn, C., Rix, H.-W., et al. 2009, *AJ*, 137, 4149
- Geier, S., Fürst, F., Ziegerer, E., et al. 2015, *Sci*, 347, 1126
- Gvaramadze, V. V., & Gualandris, A. 2011, *MNRAS*, 410, 304
- Habets, G. M. H. J., & Heintze, J. R. W. 1981, *A&A*, 46, 193
- Hills, J. G. 1988, *Natur*, 331, 687
- Hirsch, H. A.; Heber, U.; O'Toole, S. J.; Bresolin, F. 2005, *A&A*, 444, L61
- Ivezić, Ž., Branimir, S., Mario, J., et al., 2008, *ApJ*, 684, 287
- Jones, D. O., West, A. A., & Foster, J. B. 2011, *AJ*, 142, 44
- Kenyon S. J., Bromley B. C., Geller M. J., & Brown W. R. 2008, *ApJ*, 680, 312
- Kenyon S. J., Bromley B. C., Brown W. R., & Geller M. J., 2014, *ApJ*, 793, 122
- Kilic, M., Munn, J. A., Harris, H C., et al. 2006, *AJ*, 131, 582
- Kollmeier, J. A., Gould, A., Knapp, G., & Beers, T. C. 2009, *ApJ*, 697, 1543
- Kollmeier, J. A., Gould, A., Rockosi, C., et al. 2010, *ApJ*, 723, 812
- Laughlin, G., Bodenheimer, P., & Adams, F. C. 1997, *ApJ*, 482, 420
- Lépine, S., & Shara, M. M. 2005, *AJ*, 129, 1483
- Lépine, S., Rich, R. M., & Shara, M. M. 2007, *ApJ*, 669, 1235
- Li, Y., Luo, A., Zhao, G., et al. 2012, *ApJ*, 744, L24
- Lu, Y., Yu, Q., & Lin, D. N. C. 2007, *ApJ*, 666, L89
- McMillan, P. J., & Binney, J. J. 2010, *MNRAS*, 402, 934
- Morbidelli, A., Tsiganis, K., Crida, A., Levison, H. F., & Gomes, R. 2007, *AJ*, 134, 1790
- Morgan, D. P., West, A. A., Garcés, A., et al. 2012, *AJ*, 144, 93
- Munn, J. A., Monet, D. G., Levine, S. E., et al. 2004, *AJ*, 127, 3034
- Munn, J. A., Monet, D. G., Levine, S. E., et al. 2008, *AJ*, 136, 895
- Palladino, L. E., Schlesinger, K. J., Holley-Bockelmann, K. H., et al. 2014, *ApJ*, 780, 7
- Palladino, L. E., Schlesinger, K. J., Holley-Bockelmann, K. H., et al. 2014, *ApJ*, 782, 57
- Pâris, I., Petitjean, P., Aubourg, É, et al. 2014, *A&A*, 563, A54
- Perets, H. B., & Šubr, L. 2012, *ApJ*, 751, 133
- Piffi, T., Scannapieco, C., Binney, J., et al. 2014, *A&A*, 562, A91
- Reid, M. J., Menten, K. M., Zheng, X. W., et al. 2009, *ApJ*, 700, 137
- Roeser, S., Demleitner, M., & Schilbach, E. 2010, *AJ*, 139, 2440
- Roškar, R., Debattista, V. P., Stinson, G. S., et al. 2008, *ApJ*, 675, L65

- Sako, M., Romani, R., Frieman, J., et al. 2005, 22nd Texas Symposium on Relativistic Astrophysics, 415
- Sandage, A. R., & Eggen, O. J. 1959, MNRAS, 119, 278
- Savcheva, A. S., West, A. A., & Bochanski, J. J. 2014, ApJ, 794, 145
- Schlegel, D. J., Finkbeiner, D. P., & Davis, M. 1998, ApJ, 500, 525
- Sellwood, J. A., & Binney, J. J. 2002, MNRAS, 336, 785
- Sherwin, B. D., Loeb, A., & O'Leary, R. M. 2008, MNRAS, 386, 1179
- Skrutskie, M. F., Cutri, R. M., Stiening, R., et al. 2006, AJ, 131, 1163
- Schönrich, R., Binney, J., & Dehnen, W. 2010, MNRAS, 403, 1829
- Smith, M. C., Ruchti, G. R., Helmi, A., et al. 2007, MNRAS, 379, 755
- Tauris, T. M. 2015, MNRAS, 448, L6
- Theissen, C. A., & West, A. A. 2014, ApJ, 794, 146
- Theissen, C. A., West, A. A., & Dhital, S. 2015, ApJ, submitted
- Vera-Ciro, C., D'Onghia, E., Navarro, J., 7 Abadi, M. 2014, ApJ, 794, 173
- Vickers, J. J., Smith, M. C., & Grebel, E. K. 2015, AJ, 150, 77
- West, A. A., Hawley, S. L., Walkowicz, L. M., et al. 2004, AJ, 128, 426
- West, A. A., Bochanski, J. J., Hawley, S. L., et al. 2006, AJ, 132, 2507
- West, A. A., Hawley, S. L., Bochanski, J. J., et al. 2008, AJ, 135, 785
- West, A. A., Morgan, D. P., Bochanski, J. J., et al. 2011, AJ, 141, 97
- Woolf, V. M., Lépine, S., & Wallerstein, G. 2009, PASP, 121, 117
- Wright, E. L., Eisenhardt, P. R. M., Mainzer, A. K., et al. 2010, AJ, 140, 1868
- York, D. G., Adelman, J., Anderson, J. E., Jr. 2000, AJ, 120, 1579
- Zacharias, N., Finch, C. T., Girard, T. M., et al. 2013, AJ, 145, 44
- Zheng, Z., Carlin, J. L., Beers, T. C., et al. 2014, ApJ, 785, L23
- Zhong, J., Chen, L., Liu, Chao., et al. 2014, ApJ, 789, L2
- Ziegerer, E., Volkert, M., Heber, U., et al. 2015, A&A, 576, L14